Geochemistry, Geophysics, Geosystems

RESEARCH ARTICLE
10.1029/2018GC007660

Diffusion Profiles Around Quartz Clasts as Indicators of the Thermal History of Pseudotachylytes

David P. Dobson[1], **Richard W. Thomas**[1,2], **and Thomas M. Mitchell**[1]

[1]Department of Earth Sciences, University College London, London, UK, [2]Now at Department of Earth Sciences, University of Oxford, Oxford, UK

Key Points:
- Diffusion profiles are preserved around quartz survivor clasts in pseudotachylites
- There is systematic variation of diffusion length scale from edges of pseudotachylite veins to their centers
- Thermal histories can be extracted from the diffusion data

Supporting Information:
- Supporting Information S1
- Data Set S1
- Data Set S2
- Data Set S3
- Data Set S4
- Data Set S5
- Data Set S6

Correspondence to:
D. P. Dobson,
d.dobson@ucl.ac.uk

Citation:
Dobson, D. P., Thomas, R. W., & Mitchell, T. M. (2018). Diffusion profiles around quartz clasts as indicators of the thermal history of pseudotachylytes. *Geochemistry, Geophysics, Geosystems*, *19*, 4329–4341. https://doi.org/10.1029/2018GC007660

Received 14 MAY 2018
Accepted 15 OCT 2018
Accepted article online 24 OCT 2018
Published online 8 NOV 2018

Abstract Pseudotachylytes are generated by the cooling and solidification of frictional melt produced along a fault surface during seismic slip. Pseudotachylytes can, therefore, provide important constraints on thermal histories of faults during coseismic slip: survivor clast mineralogies and quenched crystallite morphologies have previously been used to constrain the peak temperatures during slip. Here we show that silicon-diffusion gradients are preserved around quartz survivor clasts and that these can be used to constrain the immediate cooling histories of pseudotachylytes after the cessation of slip. The variation of diffusion length with position in pseudotachylyte veins can be well reproduced by combining simple thermal history models with Arrhenius parameters for diffusion of appropriate magma compositions.

Plain Language Summary During earthquakes the slip on fault surfaces can be large and rapid enough to cause melting of the fault rocks. We present a new method to estimate the thermal history of the faulting process by measuring chemical diffusion profiles in quenched glass which defines some ancient exhumed fault surface.

1. Introduction

During rapid and localized coseismic fault slip in an earthquake, heat is produced at a rate significantly faster than can be diffused away from the fault plane into the wall rock (Di Toro et al., 2006, 2011; Hirose & Shimamoto, 2005; Spray, 1987). Temperatures in excess of 1400 °C can be generated where fault slip is localized to a zone less than 10 mm in width (e.g., Rice, 2006) and result in rapid generation of compositionally heterogeneous melt. The presence of such melt can cause a significant reduction in the effective coefficient of friction of the fault surface, leading to complex feedbacks between slip rate, melt content, and temperature. On cessation of seismic slip the melt rapidly cools and solidifies leaving a glassy or cryptocrystalline material on the slip surface, referred to as pseudotachylyte (e.g., Sibson, 1975). The presence of pseudotachylytes in ancient exhumed fault zones provide the only unequivocal evidence of seismic slip. Detailed studies of their geometry and habit can provide important information on the physics of the slip process, such as the thermal history of the fault plane during ancient earthquakes (Caggianelli et al., 2005; Di Toro & Pennacchioni, 2004; Jiang et al., 2015; Sibson, 1975; Tagami, 2012).

1.1. Thermometry of Pseudotachylytes

Several studies have used petrological observations of pseudotachylyte microstructure in order to infer coseismic paleo-temperatures. These include (1) the analysis of silicate glass composition (Lin, 1994), (2) two-pyroxene thermometry of microlites (Toyoshima, 1990), (3) omphacite-garnet thermometry (Austrheim & Boundy, 1994), (4) crystallization of pigeonite or mullite (Camacho et al., 1995; Moecher & Brearley, 2004), (5) mineralogy of survivor clasts (Maddock, 1983), and (6) modeling of microlite and quench textures in the pseudotachylyte (Di Toro & Pennacchioni, 2004). These techniques normally provide estimates of one point during the thermal evolution of the pseudotachylyte-bearing vein; either the peak temperature (survivor clast mineralogy; glass composition) or the temperature at the onset of crystallization (microlite geothermometry) which will proceed during a late stage of coseismic slip and take a range of values for any single event. The full thermal evolution during coseismic slip can be estimated from direct measurements during high speed friction experiments using radiation thermometry or thermocouples (e.g., Lin & Shimamoto, 1998; Ohtomo & Shimamoto, 1994; Spray, 2005; Tsutsumi & Shimamoto, 1997), or from thermodynamic models of the slip process which can be pinned to the constraints described above to model particular geological examples (Di Toro & Pennacchioni, 2004).

Table 1
Samples Used in This Study and Key Temperatures of Best-Fitting Thermal Models

Sample	Type	2*a* (mm)	T_a (°C)[a]	$\overline{T}_f$ (°C)[b]	$\overline{T}_q$ (°C)[c]
GLFZ1	Fault Vein	5.0	250	1192	1350
GLFZ2	Injection Vein	2.4	250	—[d]	1519
GLFZ3	Fault Vein	2.0	250	1519	1480
AFZ1	Fault Vein	3.2	350	1215	1278
AFZ2	Fault Vein	0.3	350	—[e]	—[e]

Note. GLFZ = Gole Larghe–Val di Genova Fault Zone; AFZ = Alpine Fault Zone.
[a]Ambient temperature of host rock. [b]Model mean vein temperature of vein at end of phase 1 (flash-heating temperature). [c]Model mean vein temperature of vein at the end of phase 2 (quench temperature). [d]The injection-vein model only has the cooling phase (phase 3). This temperature was taken as T_f from GLFZ3—see text for details. [e]Measured diffusion profiles were too short for statistical significance.

Here we describe a new method for estimating the temperature evolution of pseudotachylyte melts from chemical diffusion gradients around quartz survivor clasts. In this case observed diffusion gradients record the cooling history, from cessation of shearing until the closure temperature is reached; this corresponds to the glass transition, or freezing, temperature. Quartz clasts are chosen for several reasons. First, quartz is a common constituent of many rocks meaning that it will be present in most faulted crustal rocks. Second, it is the major mineral with the highest melting temperature in most rocks (1670–1713 °C for tridymite and cristobalite respectively; Deer et al., 1966), and it melts congruently, meaning that it is more likely to be a survivor clast than other, low-melting-temperature minerals. Third, quench overgrowths on quartz are unlikely to be mistaken for diffusion gradients. Fourth, the silica-rich glass compositions which comprise the diffusion rims will be more stable to later alteration than other, silica-poor compositions (e.g., Malow et al., 1984). Finally, measurements of chemical diffusion exist for appropriate silica-rich compositions (see Zhang et al., 2010, for a review). We do not preclude the use of diffusion gradients around other types of survivor clast, but we suggest that quartz clasts will be the most generally applicable.

In this proof-of-concept study we demonstrate the method by studying five separate pseudotachylyte veins (Table 1), from the Gole Larghe–Val di Genova Fault Zone (GLFZ) and the Alpine Fault Zone (AFZ), which display a range of pseudotachylyte vein widths, protolith rocks, and relationships to the shearing fault plane. Every studied sample is consistent with diffusion length-scale varying from the edge of veins to their centers, with diffusion haloes around clasts at the edges of veins being narrower than those in the center. We show, using a three-stage thermal evolution model, that this spatial variability contains information which can help to constrain the full thermal history of coseismic slip and subsequent quench-cooling on pseudotachylyte-bearing faults. While the simplified thermal model does not capture the full physics of the rupture and melting process, it demonstrates the richness of information contained within the diffusion profiles surrounding survivor clasts in pseudotachylytes.

1.2. Melting and Diffusion Processes

Diffusion is the physical process of movement of atoms or molecules in a material in response to a chemical potential gradient. For clasts dissolving into fault-vein melts this gradient is produced by the difference in composition between the clast and the melt. Chemical diffusion is a slow process, involving the repeated random movement of atoms to neighboring atomic positions. This requires the breaking of atomic bonds, distortion of the surrounding structure, and making new bonds and is often a thermally activated process. The final observed diffusion profile is the sum of all the random jumps of all the atoms and as such is dependent on (1) the temperature-time path of the region containing the diffusion gradient and (2) the dependence of the rate of diffusion on temperature.

In solids and simple liquids diffusion can be viewed as random jumps of individual species as they exchange positions with an appropriate vacancy (in the case of a solid) or move into a space produced by statistical fluctuations of the local environment (for simple liquids; see Dobson, 2002). The case of liquids containing structural networks, such as silica-rich magmas, is more complex with the network-forming species (Si, Al, P) showing lower diffusivities than monatomic species (alkalis and alkaline earths), sometimes by many orders of magnitude (Chakraborty, 1995; Watson, 1994). The diffusion coefficients of the network-forming species are often very similar (Dingwell, 2006), implying that their diffusion is achieved by cooperative rearrangements between the network-forming units (XO_4 tetrahedra, where X is the network-forming cation species). While there have been some measurements of the full diffusivity matrix of particular model compositions (e.g., Claireaux et al., 2016), it has been much more common to measure effective binary diffusion coefficients; this approach often works well for the network forming species.

Since the present study is concerned with diffusion of silicon away from dissolving quartz clasts, it is sufficient to use measured binary diffusion coefficients for the appropriate polymerized composition over the correct ranges in temperature to define the silicon diffusivity. The appropriate composition is defined by the ratio of nonbridging oxygens to tetrahedrally coordinated oxygens (NBO/T; see Supporting Information S1 for more

details). However, melting of polyphase rocks is not just controlled by diffusion, additionally involving the detachment of atoms from a crystal surface and diffusion of heat into the solid grain to provide the latent heat for fusion. Experiments on incipient melting and dissolution of minerals into various geological melts show a range of behaviors with any of these three processes being rate-limiting, depending on the geometry of the experimental system, degree of oversaturation, and viscosity of the melt (Shaw, 2004). In most cases, heat diffusion is not the rate-limiting step since it is so much faster than chemical diffusion (e.g., Tsuchiyama, 1986), particularly in the present case of extreme superheating. Detachment kinetics can dominate for melt compositions with low viscosities such as basanite (Shaw, 2000), lunar basalt (Thornber & Huebner, 1985), or diopside (Kuo & Kirkpatrick, 1985), but for viscous melts diffusion kinetics tends to control the rate of dissolution (Liang, 1999; Zhang et al., 1989). The careful study and synthesis of Shaw (2004) suggests that for melts with viscosities above about 1 Pa/s dissolution of solid grains is controlled by diffusion in the melt. In this case, the composition of the melt at the interface attains chemical equilibrium with the dissolving mineral grain and the diffusion profile propagates into the melt as $\sqrt{t}$. Because the initial melt is strongly out of equilibrium in pseudotachylytes, it is possible for anomalous uphill diffusion to occur—that is, some chemical components can have a flux toward regions of higher concentration of that component—meaning that the shape of the multicomponent diffusion profile is not a simple function of $\sqrt{t}$. For silicate melts this can occur for alkali components which have a strong affinity for highly polymerized melt compositions. However, Zhang et al. (1989) have shown that Si-concentration profiles still show a $\sqrt{t}$ dependence during dissolution of quartz even when alkalis are displaying uphill diffusion behavior, since it is the silica activity which defines chemical equilibrium between the melt and dissolving grain.

Pseudotachylyte melting kinetics is a special case of this general situation where flash heating causes isochemical melting of some of the minerals resulting in (1) a very heterogeneous melt and strong disequilibrium at the instant of melting, (2) a large degree of superheating, and (3) significant undersaturation in the melt of the remaining solid-clast components. The chemical heterogeneity of the starting flash melt should significantly complicate the ensuing dissolution kinetics, but since we are only interested in the concentration preserved in frozen pseudotachylytes much of this complexity can be ignored. This is because the heat source for melting is the earthquake shearing and hence, we assume here that the melt does not quench until after the shearing has ceased. In this case, while shearing is active, the melt is constantly rehomogenized by the shearing and all that is recorded in the quenched melt arises from dissolution of quartz clasts and diffusion into the homogenized melt after earthquake shearing has ceased. It is therefore reasonable in the present case of quartz survivor clasts in a pseudotachylyte in a tonalitic host rock to measure silica diffusion gradients and assume that the rate-limiting step of quartz dissolution is chemical diffusion in the melt (see Supporting Information S1 for further discussion).

There is, however, one further confounding factor associated with melt cooling: crystallization. There are three situations to consider in the present case: (1) homogeneous nucleation and growth of quench crystals (microlites) within the melt, (2) heterogeneous nucleation and quench overgrowth of the survivor clasts, and (3) subsequent alteration and devitrification of the pseudotachylyte glass. Each of these processes will perturb the local chemical composition, adding noise to the observed diffusion gradients. (1) In the case of microlites, the size of the crystal and length-scale of the diffusion gradient is small and, for many purposes, the bulk composition can be determined by chemical analysis of an area which is sufficiently large to contain a statistically significant number of microlites. This is not the case in the present study where the diffusion gradients of interest are likely to be similar in length to microlite sizes. Nucleation and growth of microlites in the GLFZ pseudotachylytes is the focus of the study by Di Toro and Pennacchioni (2004) who use the geometries of quench-crystal aggregates as indicators of peak temperatures. It is sufficient here to note that microlites are less common in the silica-rich compositions immediately surrounding quartz clasts (Figures 1b and 1d) and we measure profiles around clasts which are not immediately surrounded by microlites. (2) Quench overgrowth on quartz of dmisteinbergite, the high-temperature polymorph of $CaAl_2Si_2O_8$, has been observed in GLFZ pseudotachylytes (Nestola et al., 2010). Due to the large compositional difference between the quartz and the quench overgrowth, this is readily identified in SEM images (e.g., Figure 1b) and compositional profiles and such grains are readily avoided. (3) Late-stage alteration and devitrification of geological glass is common in many systems, with silica-poor compositions more susceptible than silica rich systems. The products of these reactions are often cryptocrystalline and can contain a range of phases, from the equilibrium phase assemblage of the glass through to low-grade metamorphic minerals and clays

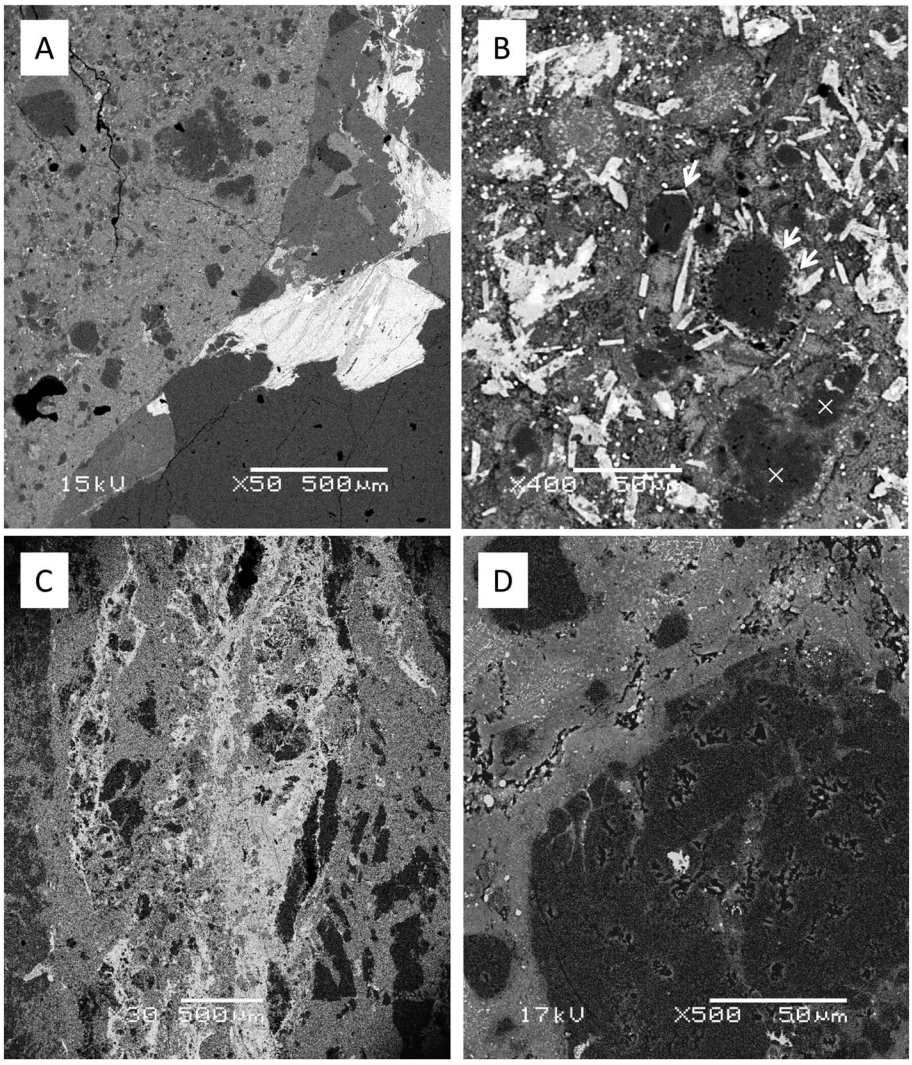

Figure 1. Backscattered electron images of samples of Gole Larghe–Val di Genova Fault Zone pseudotachylytes. (a)–(b) Sample GLFZ2 from an injection vein. The wall rock is virtually undamaged (a). (c)–(d) Sample GLFZ3 from a fault vein showing progressive damage of the wall rock toward the vein. Quartz clasts are dark grains which sometimes show overgrowths of dmisteinbergite (indicated by arrows in (b)). diffusion profiles were only measured around clasts which showed no evidence of quench overgrowth and were far from regions containing microlites, such as those marked with a cross in (b) and those shown in (d).

(Kirkpatrick & Rowe, 2013). Analytical techniques with very small analytical spot sizes (such as TEM and nanoSIMS techniques) will be particularly sensitive to noise from devitrification and alteration products which often have nanometric grainsizes but traditional tungsten-filament SEM techniques with ~1 μm analytical volume allow a degree of spatial averaging of the cryptocrystalline devitrification products.

2. Samples

2.1. The GLFZ

The samples from the GLFZ studied here were a subsample of those used by Mitchell et al. (2016). The GLFZ is a 20 km, E–W-trending, strike-slip fault which crosscuts the whole Northern Adamello Tertiary batholith in the Italian Southern Alps (Di Toro et al., 2004). The Adamello massif is predominantly of granodiorite-tonalite composition, intruding thrust nappes composed of pre-Alpine metamorphic basement (Smith et al., 2013). The fault zone cuts across medium-grained tonalites belonging to the Avio intrusion (Bianchi et al., 1970; Mitchell et al., 2016) of the composite Adamello batholith. Peak temperatures during seismic slip have

been estimated to be ~1450 °C from compositions of melted clasts (Di Toro & Pennacchioni, 2004) and the presence of the high-temperature hexagonal polymorph of $CaAl_2Si_2O_8$, dmisteinbergite (Nestola et al., 2010). Ambient conditions of the host tonalite during formation of the pseudotachylyte were 0.25–0.3 GPa and 250–300 °C. Pseudotachylyte-bearing fault surfaces occur at meter-scale spacings, having exploited pre-existing zones of low cohesion, and injection veins at high angles to the fault veins are common (Mitchell et al., 2016). Three samples were chosen for the present study. Two parallel-sided fault-vein pseudotachylytes with widths of approximately 2 and 5 mm and one injection-vein pseudotachylyte were chosen. The injection-vein pseudotachylyte had a complex geometry but a region which was approximately planar, with a width of about 2.5 mm, was chosen since this would be best approximated by the 1-dimensional finite-difference thermal model used here. The pseudotachylytes contain $<$20% clasts of quartz and (minor) feldspar/dmisteinbergite. The matrix is extensively devitrified and altered to very fine grained mixtures of epidote+chlorite, but in the silica-rich diffusion halos around quartz clasts alteration is less extensive and the matrix around quartz clasts appears homogeneous in the scanning electron microscope in back-scattered imaging mode (Figure 1).

2.2. The AFZ

The AFZ samples used here are hosted in mylonites and are a subsample of those studied in Mitchell et al. (2016). The AFZ of New Zealand is a major transcurrent fault that is still active between the Pacific and the Indo-Australian plates. Slip began in the mid-Oligocene (30 Ma) and continued through the late Miocene (10 Ma), when change in the orientation of the slip vector then led to oblique compression that was responsible for the uplift of the Southern Alps (Carter & Norris, 1976). The mylonitic foliation in the fault zone is presently dipping 40–80° to the east, while the stretching lineation plunges in a direction subparallel to the present-day slip vector between the Indo-Australian and Pacific plates. Present-day, oblique convergence at the AFZ boundary results in dextral strike-slip, vertical uplift, and westward over-thrusting of schists of the Southern Alps onto the West Coast sequence (Bossiére, 1991). The source of the mylonites is a quartzo-feldspathic Alpine Schist, resulting from amphibolite-facies metamorphism of a metasedimentary protolith (part of the Aspiring Lithologic Association of the Torlesse Terrane; Norris & Craw, 2013). Its mineralogy is ~40% quartz, ~35% oligoclase feldspar, ~15% mica (biotite + muscovite) with minor accessory minerals. The minerals are generally well mixed and dispersed, with only occasional bands of quartz/quartzo-feldspathic material which define a weak lineation. Pseudotachylyte veins occur on slip planes parallel to the foliation, with a centimeter-to-tens of centimeter spacing. Due to the highly anisotropic mechanical properties of the mylonite (Mitchell et al., 2016) injection veins are rare. Although this does not affect the results of the present study, it does mean that only fault-vein pseudotachylytes were studied from the AFZ. Ambient conditions of the host rock during formation of the pseudotachylyte were ~0.1 GPa and 300–350 °C (Toy et al., 2011). Two parallel-sided samples were chosen, with widths of approximately 3.2 and 0.3 mm. Clasts within the pseudotachylytes are dominated by quartz and feldspar and constitute ~30 vol% of the pseudotachylytes.

3. Methodology

3.1. Measurement of Diffusion Profiles

Samples were cut perpendicular to all pseudotachylyte veins and polished sections prepared, finishing with 0.3 μm alumina. The polished sections were cleaned in distilled water in an ultrasonic bath, wiped over with clean isopropanol, and coated with carbon (to about 15 nm thickness) for analysis by scanning electron microscope. A JEOL JSM-648OLV Scanning Electron Microprobe was used with operating conditions of 15 kV accelerating voltage, with a spot size of 20, corresponding to a beam current of approximately 10 nA. The source was a traditional tungsten-filament giving a resolution for imaging of ~0.1 μm. Characteristic elemental X-ray fluorescences were detected by a Si-drift detector running under Oxford INCA X-sight software. Compositional profiles, typically of ~40 μm in length, were measured from quartz survivor clasts into the surrounding cryptocrystalline pseudotachylyte using the line scan feature of the INCA software, at 512 points per line, with 50 frames collected, corresponding to ~30 min data collection time along the entire profile. The spacing of analysis points using this protocol was significantly smaller than the analytical volume of the beam and so a beam-shape convolution was necessary when treating the data (see below). Profile lines were chosen to be perpendicular to the surface of the clast to reduce any spurious

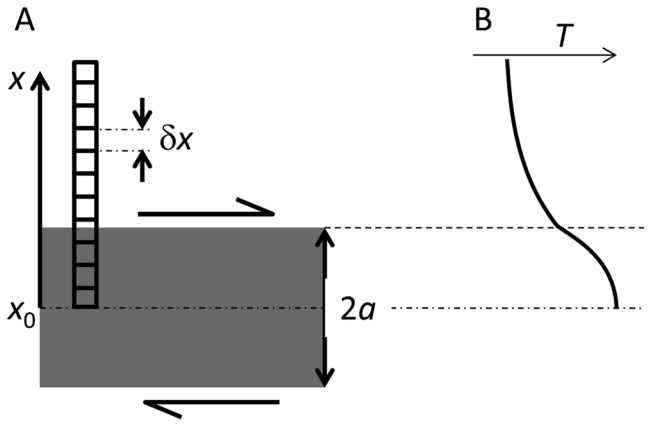

Figure 2. Half-space model of a frictionally heated fault zone. (a) Cartoon showing the details of the finite difference model. The shearing zone is shown in gray and has a width of 2*a*. The model is symmetrical about the central plane of the fault, located at X_0. (b) Cartoon of temperature profile generated by shear on the fault under conditions of constant stress, velocity, and coefficient of friction, corresponding to phase 1 of the model (see text for details).

lengthening of the measured profile, however it was not possible to ensure that the tangent plane of the clast surface at the point of the analytical line was perpendicular to the polished section surface. We therefore collected multiple profiles from each clast and measured multiple clasts at each position and consider the shortest observed profiles to be most representative of the true diffusion profile at each point. This process was repeated at intervals across the width of the pseudotachylyte vein in order to determine the dependence of diffusion on position in the vein.

Line scan data, comprising elemental X-ray counts for Na, Mg, Al, Si, K, Ca, Ti, and Fe at each analytical point, *x*, were collected for diffusion fitting. An apparent silicon concentration, [Si], defined as $C_{Si}/\Sigma C_m$ where C_m is the X-ray count for element m, was fitted. A constant composition boundary condition exists at the edge of the quartz clasts and the diffusion profile is fitted by Crank (1975; equation 3.13):

$$\frac{[\mathrm{Si}]-[\mathrm{Si}]_1}{[\mathrm{Si}]_0-[\mathrm{Si}]_1}=\mathrm{erf}\frac{x}{2\sqrt{\int D\mathrm{d}t}}. \tag{1}$$

In implementing this fit, there are three independent variables and one dependent variable: (x_0), the position of the start of the profile; ($[\mathrm{Si}]_0$, $[\mathrm{Si}]_1$), the compositions in the solid and the liquid far from the profile; and $\int D\mathrm{d}t$, the diffusion length scale. The chemical diffusivity, *D*, is a strong positive function of temperature, so the diffusion length scale contains information about the thermal history of the fault.

An additional complication arose due to the short lengths of the measured profiles—the finite analytical volume is significant compared to the length of the diffusion profile. This was corrected for by adding a Gaussian convolution to the analytical solution and the convolved profile was then fitted to the observations using a linear least-squares method. The size of the Gaussian profile was determined by measuring compositional profiles across solid mineral-mineral contacts in the country rock which should be infinitely sharp at the resolution of the present measurements. Several interfaces were measured and the mean of the best-fitting Gaussians was used in the beam convolution of the diffusion profiles. This was implemented as a weighted box-car average with the mean Gaussian providing the weighting.

3.2. Thermal and Diffusion Modeling

In order to invert the observed diffusion gradients for pseudotachylyte vein thermal histories we implemented a simple numerical model of the veins (of width 2*a*), corresponding to the analytical solutions for uniform shear-heating in a fault zone previously described (Cardwell et al., 1978; Lachenbruch, 1986; Murakami, 2010). The model comprised a 1-D finite difference numerical solution to the infinite-sheet dyke cooling problem (Carslaw & Jaeger, 1959; Figure 2). This was modified for fault-vein models to allow heating within the sheet, $0 < X < a$, from shear dissipation according to the formula:

$$Q_s = \mu\tau u, \tag{2}$$

where Q_s is the heat flux per unit area, μ is the coefficient of friction, τ is the shear stress (6 MPa), and *u* is the slip velocity (1 m/s $< u <$ 2 m/s). Heat is conducted away from the shearing region at each position, X, according to the equation:

$$Q_c = -K\mathrm{d}T(X)/dX, \tag{3}$$

where *K* is the thermal conductivity. For a model comprising boxes of unit area and width ΔX, the change in temperature at each time step is given by:

$$\Delta T = C_p\rho(Q_s+Q_c)\Delta t = C_p\rho(\mu\tau u\Delta X/a + (T_{n-1}-2T_n+T_{n+1})/2\Delta X)\Delta t \quad 0<X<a; \tag{4a}$$

$$\Delta T = C_p\rho Q_c\Delta t = C_p\rho(T_{n-1}-2T_n+T_{n+1})/2\Delta X)\Delta t \quad a<X, \tag{4b}$$

where the subscript, *n*, denotes the *n*th box with $n = 1$ at the center of the vein. The heat capacity, C_p, density,

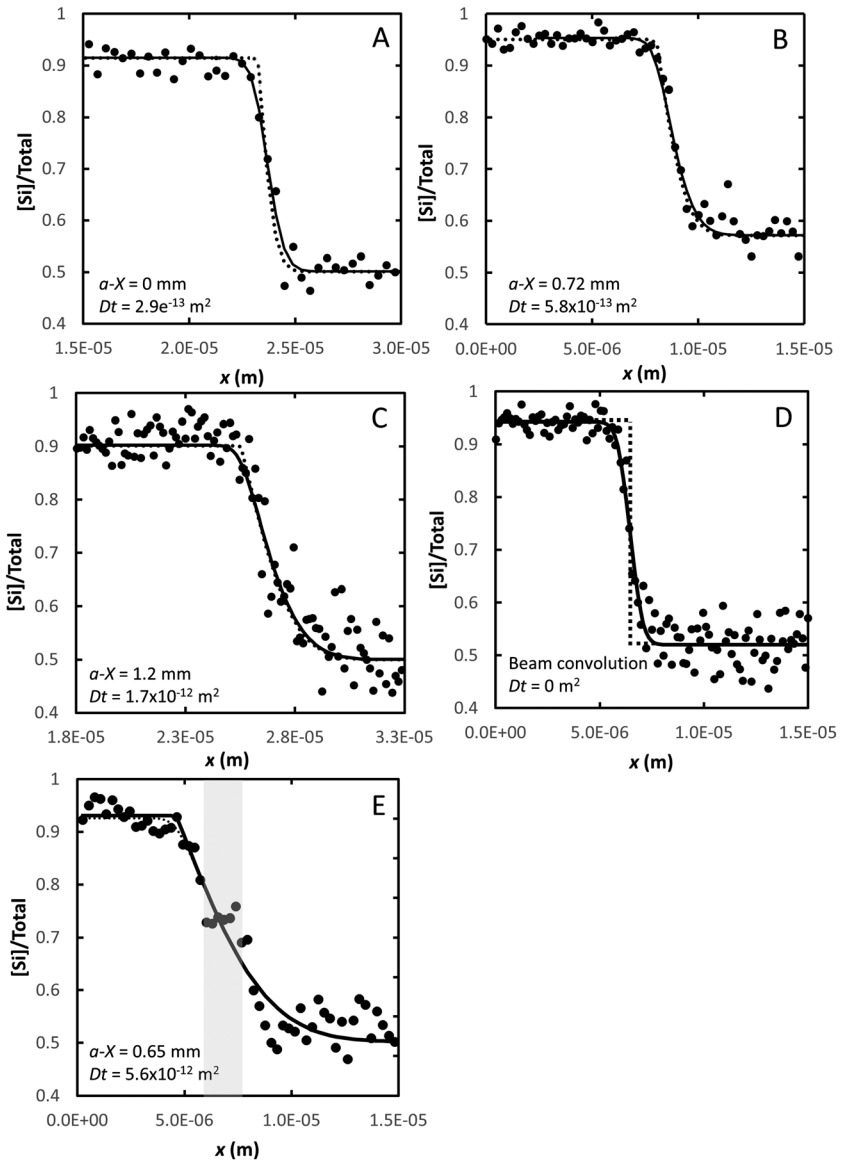

Figure 3. Diffusion profiles from pseudotachylyte injection vein sample GLFZ2. (a)–(c) Profiles collected at different distances from the edge of the vein (*X-a*). (d) Profile collected across a quartz-feldspar interface in the host rock showing the contribution of the finite beam size. Solid points are the analytical values, dashed lines are the best fitting diffusion profiles and the solid lines are the fitted diffusion profiles including the Gaussian beam-shape convolution. (e) Diffusion profile collected from a quartz grain which had a quench overgrowth of dmisteinbergite (region marked in gray). The overgrowth shows a constant composition intermediate to the quartz clast and the melt. Fitting a diffusion profile to this leads to erroneously large apparent diffusivities.

ρ, and thermal conductivity are typical values for acid igneous rocks (0.79 $J{\cdot}g^{-1}{\cdot}K^{-1}$, 2.7 × 10^6 g/m^3, and 2.5 $W{\cdot}m^{-1}{\cdot}K^{-1}$, e.g., Eppelbaum et al., 2014) and Δt is the size of each time step. This formulation supplies heat evenly across the shearing region and results in a temperature profile of the form shown in Figure 2b while shear is active.

We divide the model into three time periods. Phase 1: the entire system starts at the background temperature (250 °C for GLFZ samples and 350 °C for AFZ samples) and the shearing region is entirely solid; the coefficient of friction is set to 0.6 during this period, in accordance with laboratory measurements (Hirose & Shimamoto, 2005; Spagnuolo et al., 2016). Phase 2: once flash melting occurs (here we assume this happens after 1 s of shearing) the melt lubricates the shearing region and the effective coefficient of friction is instantaneously reduced. Here we have chosen a value of a weakening of 67% (i.e., μ = 0.2) post-melting. This weakening

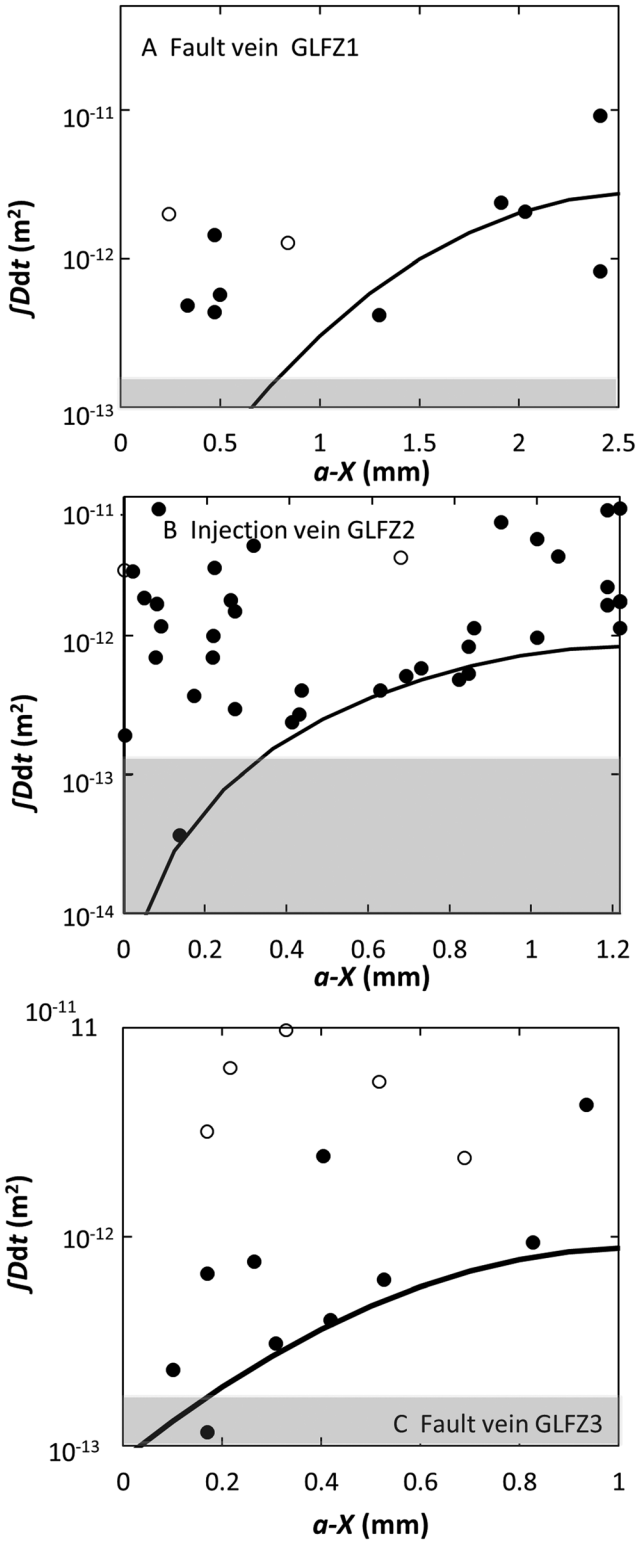

Figure 4. Observed (symbols) and modeled (solid line) chemical diffusion profile lengths, $\int Ddt$, around quartz survivor clasts for GLFZ fault-vein (a), (c) and injection vein (b) pseudotachylyte samples. Open symbols are for diffusion profiles which, on close inspection, showed evidence for quench overgrowth. The gray region marks the limit of instrumental resolution. GLFZ = Gole Larghe–Val di Genova Fault Zone.

is somewhat larger than that observed (~50%) from many laboratory experiments (Hirose & Shimamoto, 2005), however the confining pressure acting on the natural samples studied here was higher than in laboratory experiments meaning that the weakening of the effective coefficient of friction should be larger than in the experiments (Di Toro et al., 2004; Fialko & Khazan, 2005; Nielsen et al., 2010). This phase lasts for the same duration as the first phase. Phase 3: the velocity is instantaneously reduced to zero and the system evolves by heat conduction alone. While this does not include a deceleration phase the effect that this would have on heat generation is to first order mimicked by the large reduction in effective friction used here. For all but the widest vein studied here, this results in a peak temperature at the center of the shearing region at the end of phase 1, but regions further out in the shearing region continue to heat up during phase 2. The second phase is necessary to model the spatial dependence of diffusion-profile length in the fault-vein pseudotachylyte. The widest vein continues to heat up at all positions during phase 2, suggesting that an even more extreme melt-lubrication might have been appropriate for this instance.

For injection veins just phase 3 is used, corresponding to the dyke cooling problem and giving results consistent with the analytical solution of Di Toro and Pennacchioni (2004) as implemented in Mitchell et al. (2016). The initial temperature profile within the injection vein is set to a constant value which corresponds to the mean temperature of the shear vein at the end of phase 1. This implies that injection veins formed at the peak temperature of flash heating and that the injected material was turbulently mixed during the injection process.

The thermal model therefore has effectively four variables: background temperature, vein width, heat production rate, and duration of slip. The first two of these are defined by geothermometry and geometry of the individual samples, leaving two adjustable parameters. The heat production rate, Q_s, depends on the shear velocity, shear stress, and coefficient of friction; none of these are known for the ancient faults and they are fully correlated. We chose not to vary the coefficient of friction (0.6 for phase 1 and 0.2 for phase 2) or shear stress (6 MPa) and to use the slip velocity and the duration as the adjustable parameters. This returns a temporal evolution of the temperature at each grid point in the fault.

The diffusion length scale, $\int Ddt$, at each grid point is then calculated by numerical integration over time for just phase 3, assuming an Arrhenius temperature dependence for diffusivity with parameters ($D_0 = 3.08 \times 10^{-4}$ m^2/s and $\Delta H = 268$ kJ/mol) taken from the literature for diffusion of trivalent cations in dacitic melt (Baker, 1992), as appropriate for the mean NBO/T value for these pseudoctachylytes (e.g., Mysen, 1983). Neglecting phases 1 and 2 in calculating the diffusion history of the fault veins implies that any diffusion gradients around clasts are destroyed by shearing during these phases. This is strictly true for diffusion perpendicular to the shear plane and is likely to be true also for other directions since rotation of clasts in the shearing melt will locally perturb any laminar flow in the shearing region and tend to destroy diffusion gradients (e.g., Lavallée et al., 2012). Diffusion was considered to cease once the temperature dropped below the solidus of the system. This was taken to be 750 °C here, but the simulations are not sensitive to this value since chemical diffusion follows an Arrhenius relationship with the majority of diffusion

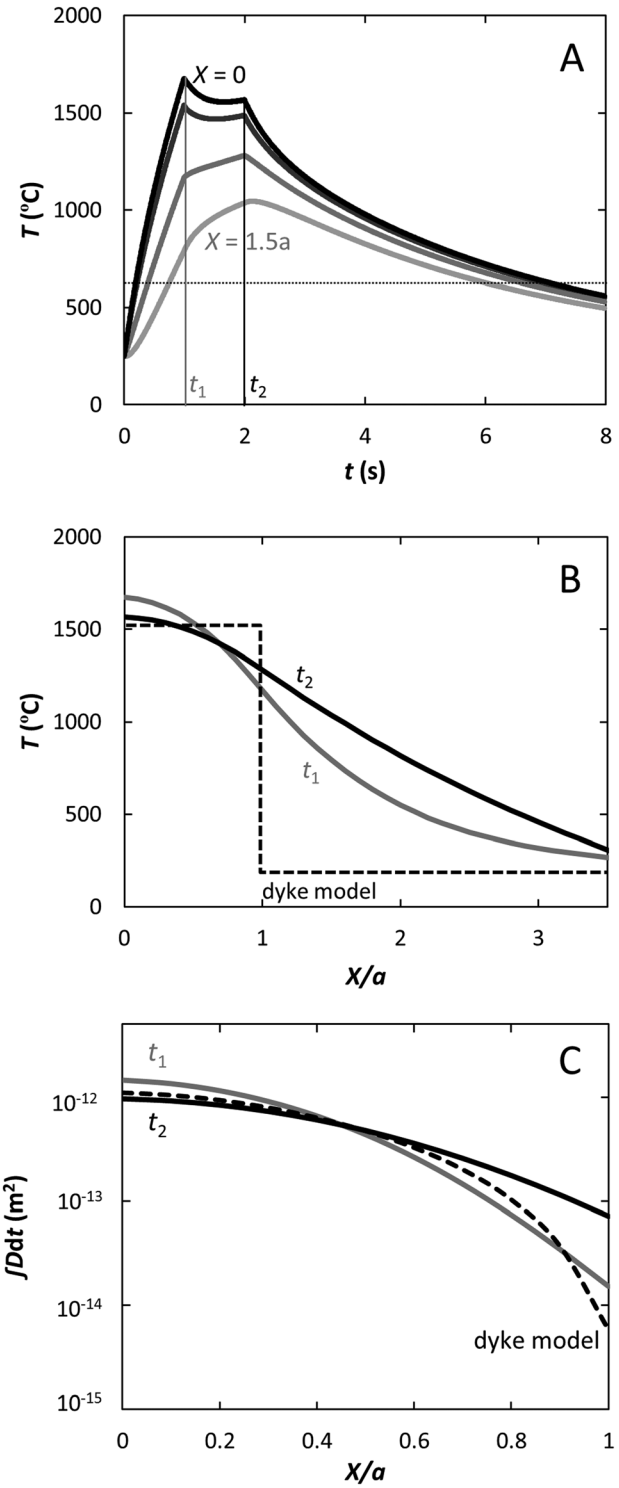

Figure 5. Temperature profiles from the best-fitting thermal model for sample GLFZ3. (a) Thermal evolution with time at distances $X = 0$, $0.5a$, $1a$, and $1.5a$ from the center of the vein with a half-width of a. (b) Profiles across the model at times t_1 (black line) and t_2 (gray line), and for the dyke injection model used for futting sample GLFZ2. (c) Diffusion profiles generated by integrating the temperature-dependent diffusivity, $\int D dt$, over the conductive cooling history starting with the temperature profiles shown in (b). See text for further details of the numerical modeling.

occurring at the highest temperatures. In developing the model we assume that survivor clasts remain isothermal to the surrounding melt during the cooling phase. For large clasts this is an invalid assumption (Bizzarri, 2014) but for the present study (with clast diameters ≤100 μm) thermal lag within clasts is short (≪0.1 s) compared with the heating and cooling rates of the veins.

The calculated diffusion length scales are then compared to the shortest observed profiles at each analysis position by interpolating between grid points to determine the model value for each analysis position. Values of velocity and time were varied to minimize the squared missfits between the observations and models with the reduced chi-square statistic, χ^2_v, as a measure of goodness of fit. A sensitivity analysis (Supplementary section S2) shows that fits for the fault veins are sensitive to both peak temperature and time taken to reach peak temperature, with strong correlation between the two, but that fits for injection veins are only sensitive to temperature. The best model fit is achieved through simultaneously fitting the injection vein and fault vein samples, with $\chi^2_v = 0.35$.

4. Results

4.1. Diffusion Profiles

Figure 3 shows representative diffusion profiles in injection vein sample GLFZ2 collected at various distances, *a-X*, from the edge of the vein, along with a profile from an interface between a quartz grain and a feldspar grain in the host hock to show the effect of the finite beam size. There is a qualitative increase in diffusion length scale, $\int D dt$, with distance from the edge of the vein. Shorter profiles show a significant contribution from the beam profile: the best fit, including the beam-profile convolution, to the shortest diffusion profile shown has a length scale of 2.9×10^{-13} m^2, whereas if this convolution is neglected the best-fitting profile has twice as large length scale, of 4.7×10^{-13} m^2. The profile across the clast with an overgrowth of dmisteinbergite shows a clear plateau in silica concentration in the overgrowth region and the fitted diffusion profile is considerably longer than *clean* profiles at similar positions (*a-X*).

Figure 4 shows the measured diffusion lengths as a function of distance (points) from the vein edge, along with the model fits (lines) for GLFZ samples. The gray regions denote where profiles are too short for significance at the current analytical resolution. To first order, all of the samples show considerable similarities. There is a large scatter in measured diffusion length scales but the minimum length scales at each point define a tightly bounded curve which decreases in magnitude as the edge of the vein (*a-X* = 0) is approached. The scatter is mainly due to the fact that most quartz clasts are not sectioned at their centers meaning that diffusion profiles are sampled obliquely to the diffusion distance. We know of no process whereby measured apparent diffusion profiles can be shorter than the true diffusion profile so we consider that the shortest profile at any point is representative of the true value. In this case, the fact that the lower-bounding values diminish as the edge of the vein is approached implies that the edges of veins either (1) did not reach as high a temperature as or (2) cooled more rapidly than the centers of veins. Such behavior is expected from (1) models of shear-heating of veins (Cardwell et al., 1978) and (2) the analytical solution for dyke cooling (Carslaw & Jaeger, 1959).

All profiles for samples from the AFZ were close to, or below, the instrumental resolution (see Figure S4).

4.2. Thermal Evolution Models

Sample temperature profiles from the model fit to GLFZ3 are plotted in Figure 5. Peak temperature is reached in the center of the vein at the end of phase 1 (at 1 s in Figure 5a) but the edge of the vein continues to heat during melt-lubricated shearing (phase 2) reaching a maximum temperature at 2 s. This phase of melt-lubricated slip produces a broader temperature profile across the vein, with a lower maximum temperature at the onset of development of diffusion profiles (Figure 5b). This then results in a smaller range of diffusion length scales (Figure 5c) across the vein, ranging from 9.7×10^{-13} m^2 at the center of the vein to 7.2×10^{-14} m^2 for the three-stage model compared to 1.5×10^{-12} m^2–1.5×10^{-14} m^2 for a model where phase 2 is omitted. The dyke cooling model, corresponding to the case for injection veins, has an even stronger spatial dependence of diffusion length scales (Figure 5c) since the host rock has received no conductive heating prior to injection and the melt at the edge of the vein quenches instantly.

Figure 4 shows that the full, three stage, thermal evolution models for the GLFZ samples fit the data very well; there is no model solution which fits the fault-vein data as well if the melt-lubricated phase is not included, showing that the diffusion data contain information about the full thermal history of the melt-producing slip event. Modeled temperatures at the start of phase 3 (the mean quench temperature, T_q, when the diffusion profile starts to develop) range from 1350 to 1520 °C (Table 1). The injection vein sample (GLFZ2) which is fitted by the dyke-cooling model (phase 3 only) requires the highest value of T_q, corresponding to the mean temperature at the end of phase 1 (T_f) of model GLFZ3 (shown in Figure 5). It seems reasonable that injection veins are intruded into the host rock at the peak temperature when melting rates (and hence overpressures in the fault) will be highest and before melt-lubrication allows the fault surface to cool. Additionally, the formation of injection veins removes melt from the sliding surface, reducing the melt-lubrication effect and will, therefore, allow the faulting surface to maintain its peak temperature longer. Sample GLFZ1, which is over twice the width of the other two samples from this locality, requires a lower quench temperature to fit the data, but this is the worst constrained of these three samples with the most sparse data set. The modeled temperatures for all of the GLFZ samples are within 100 °C of previous estimates of peak temperatures of 1450 °C for pseudotachylytes from this region (Di Toro & Pennacchioni, 2004; Nestola et al., 2010), which we consider to be in good agreement given the simplicity of the model.

Both of the samples from the AFZ show significantly shorter diffusion length scales (Figure S4) than GLFZ samples, at 2×10^{-13} m^2, or less, indicating a lower quench temperature. The modeled quench temperature for sample AFZ1, which is similar in thickness to GLFZ2 and GLFZ3, is 200 °C lower than for these samples, at 1280 °C. This is at the upper range of estimates of temperatures recorded by AFZ pseudotachylytes (750–1200 °C; Wallace, 1976; Warr & van de Pluijm, 2005). The case is worse for sample AFZ2, which is approximately one tenth the thickness of the other samples and the minimum diffusion length scales are well below significance. The curve in this case is for a model which produces a quench temperature the same as the AFZ1 model (1280 °C) and is not a fit to the data—the best-fitting model requires a quench temperature of 1550 °C. There is possibly a good physical reason why our model has overestimated the temperature of AFZ samples, which we will discuss below, but we note that the diffusion length scales in this sample are close to, or below, the instrumental resolution so we have less confidence in the fitted model parameters for this sample.

5. Discussion and Conclusion

The present study shows that pseudotachylytes contain diffusion halos around quartz survivor clasts and that the spatial variability of these diffusion profiles shows structure which can be used to constrain thermal models of the shearing and quenching process. While model temperatures at the cessation of shearing agree well with previous estimates for GLFZ samples, the agreement is not so good for the AFZ samples. We suggest that this may be due to the chemical diffusivity we used in the present study being too small. The AFZ pseudotachylytes show a greater variation in NBO/T across the diffusion gradients, from 0.03 at the interface with the quartz clast to a mean value of 0.6 (similar to subalkaline basalts; Mysen, 1983) in the far field. In this case the use of a single set of compositional-independent diffusivity parameters might not be appropriate and the analysis would require explicit numerical modeling of each diffusion profile including composition dependencies of chemical diffusivities. The current diffusion data for the AFZ do not warrant this, being close to

the resolution limit of the analytical technique. Additionally, previous estimates (700–800 °C) of peak temperatures for AFZ pseudotachylyte are based on dehydration-melting temperatures of the abundant hydrous minerals (biotite and amphibole) which would have been present in the host rock during the slip event. Water not only reduces the melting temperature of rocks but it also acts as a network-breaking component in silicate melts, decreasing the viscosity and increasing chemical diffusivity. Our use of the value for dry dacite therefore places an absolute upper bound on quenching temperatures for the AFZ samples.

Further improvements could be made in future studies: (1) higher spatial resolution is required in analyzing diffusion profiles in very thin veins—this could be readily achieved using transmission electron microscope or nanoSIMS methods. But there is a concomitant trade-off between spatial resolution and noise in the diffusion profile due to the inherent chemical variability created by devitrification and alteration products. (2) We have neglected the complexity of nonequilibrium dissolution processes and compositional-dependent diffusion in fitting the diffusion halos around quartz clasts. Studies which measure diffusion in flash-heated quartz-feldspar mixtures (e.g., Yuguchi et al., 2012) could provide better constraints on diffusivities, but none currently exist at sufficiently high temperatures. In practice, the fits using simple composition-independent diffusion coefficients were perfectly adequate to fit the observed profiles and there are good reasons why this is so (Supporting Information section 1). (3) We used a simple thermal model, which ignores much of the physics of seismogenic slip, in order to demonstrate that the observed diffusion gradients contained information which of itself could help to constrain thermal histories of pseudotachylytes. Despite the simplifications of this proof-of-concept study we have shown that the spatial variation of diffusion profiles around quartz survivor clasts in pseudotachylytes are sensitive to the peak temperature and thermal histories of the slip events which produced the pseudotachylytes. Diffusion profiles could therefore be used to constrain key seismic parameters of ancient faulting events if combined with thermal evolution models which capture the full physics of the faulting process.

Acknowledgments
D.P.D. acknowledges funding from the Natural Environment Research Council (NE/K002902/1; NE/L006898) and a Bessel Award from The Alexander von Humboldt Foundation. TMM acknowledges Natural Environment Research Council grant NE/M004716/1. This work was, in part, performed as a master's project: R.T. is grateful for the support from the Glamorgan Education Trust. All the data used are available in the Supporting Information.

References

Austrheim, H., & Boundy, T. M. (1994). Pseudotachylytes generated during seismic faulting and eclogitization of the deep crust. *Science*, *265*, 82–83. https://doi.org/10.1126/science.265.5168.82

Baker, D. R. (1992). Tracer diffusion of network formers and multicomponent diffusion in dacitic and rhyolitic melts. *Geochimica et Cosmochimica Acta*, *56*, 617–631. https://doi.org/10.1016/0016-7037(92)90086-X

Bianchi, A., Callegari, E., & Jobstraibizer, P. G. (1970). I tipi petrografici fondamentali del plutone dell'Adamello. *Memorie degli Istituti di Geologia e Mineralogia dell'Universita di Padova*, *27*, 1–148.

Bizzarri, A. (2014). The Destiny of a clast within a molten Pseudotachylyte vein. *Bulletin of the Seismological Society of America*, *104*, 2399–2411. https://doi.org/10.1785/0120140084

Bossiére, G. (1991). Petrology of pseudotachylytes from the Alpine Fault of New Zealand. *Tectonophysics*, *196*, 173–193. https://doi.org/10.1016/0040-1951(91)90295-4

Caggianelli, A., Lorenzo, S. D., & Prosser, G. (2005). Modelling the heat pulses generated on a fault plane during co-seismic slip: Inferences from the pseudotachylytes of the Copanello cliffs, (Calabria, Italy). *Tectonophysics*, *405*, 99–119. https://doi.org/10.1016/j.tecto.2005.05.017

Camacho, A. H., Vernon, R., & Fitz Gerald, J. D. (1995). Large volumes of anhydrous pseudotachylyte in the Woodroffe Thrust, eastern Musgrave Ranges, Australia. *Journal of Structural Geology*, *17*, 371–383. https://doi.org/10.1016/0191-8141(94)00069-C

Cardwell, R. K., Chinn, D. S., Moore, G. F., & Turcotte, D. L. (1978). Frictional heating on a fault zone with finite thickness. *Geophysical Journal of the Royal Astronomical Society*, *52*, 525–530. https://doi.org/10.1111/j.1365-246X.1978.tb04247.x

Carslaw, H. S., & Jaeger, J. C. (1959). *Conduction of heat in solids*. Oxford: Oxford University Press.

Carter, R. M., & Norris, R. J. (1976). Cainozoic history of southern New Zealand: An accord between geological observations and plate-tectonic predictions. *Earth and Planetary Science Letters*, *31*, 85–94. https://doi.org/10.1016/0012-821X(76)90099-6

Chakraborty, S. (1995). Diffusion in silicate melts. In: Stebbins JF, McMillan PF, Dingwell DB (eds) structure, dynamics and properties of silicate melts. *Mineralogical Society of America Reviews in Mineralogy*, *32*, 411–503.

Claireaux, C., Chopinet, M.-H., Burov, E., Gouillart, E., Roskosz, M., & Toplis, M. J. (2016). Atomic mobility in calcium and sodium aluminosilicate melts at 1200 °C. *Geochimica et Cosmochimica Acta*, *192*, 235–247. https://doi.org/10.1016/j.gca.2016.07.032

Crank, J. (1975). *The mathematics of diffusion* (2nd ed.). Oxford: Clarendon Press.

Deer, W. A., Howie, R. A., & Zussman, J. (1966). *An introduction to the rock forming minerals* (pp. 340–355). Harlow, UK: Logman.

Di Toro, G., Goldsby, D. L., & Tullis, T. E. (2004). Friction falls towards zero in quartz rock as slip velocity approaches seismic rates. *Nature*, *427*, 436–439. https://doi.org/10.1038/nature02249

Di Toro, G., Han, R., Hirose, T., De Paola, N., Nielsen, S., Mizoguchi, K., Ferri, F., et al. (2011). Fault lubrication during earthquakes. *Nature*, *471*, 494–498. https://doi.org/10.1038/nature09838

Di Toro, G., Hirose, T., Nielsen, S., Pennacchioni, G., & Shimamoto, T. (2006). Natural and experimental evidence of melt lubrication of faults during earthquakes. *Science*, *311*(5761), 647–649. https://doi.org/10.1126/science.1121012

Di Toro, G., & Pennacchioni, G. (2004). Superheated friction-induced melts in zoned pseudotachylytes within the Adamello tonalites (Italian Southern Alps). *Journal of Structural Geology*, *26*, 1783–1801. https://doi.org/10.1016/j.jsg.2004.03.001

Dingwell, D. B. (2006). Transport properties of magmas: Diffusion and rheology. *Elements*, *2*, 281–286. https://doi.org/10.2113/gselements.2.5.281

Dobson, D. P. (2002). Self-diffusion in liquid Fe at high pressure. *Physics of the Earth and Planetary Interiors*, *130*, 271–284. https://doi.org/10.1016/S0031-9201(02)00011-0

Eppelbaum, L., Kutasov, I., & Pilchin, A. (2014). *Applied geothermics, lecture notes in Earth system sciences* (p. 267). Berlin Heidelberg: Springer-Verlag. https://doi.org/10.1007/978-3-642-34023-9_2

Fialko, Y., & Khazan, Y. (2005). Fusion by earthquake fault friction: Stick or slip? *Journal of Geophysical Research*, *110*, B12407. https://doi.org/10.1029/2005JB003869

Hirose, T., & Shimamoto, T. (2005). Growth of molten zone as a mechanism of slip weakening of simulated faults in gabbro during frictional melting. *Journal of Geophysical Research*, *110*, 520–522. https://doi.org/10.1029/2004JB003207

Jiang, H., Lee, C.-T. A., Morgan, J. K., & Ross, C. H. (2015). Geochemistry and thermodynamics of an earthquake: A case study of pseudotachylytes within mylonitic granitoid. *Earth and Planetary Science Letters*, *430*, 235–248. https://doi.org/10.1016/j.epsl.2015.08.027

Kirkpatrick, J. D., & Rowe, C. D. (2013). Disappearing ink: How pseudotachylytes are lost from the rock record. *Journal of Structural Geology*, *52*, 183–198. https://doi.org/10.1016/j.jsg.2013.03.003

Kuo, L.-C., & Kirkpatrick, R. J. (1985). Kinetics of crystal dissolution in the system diopside-forsterite-silica. *American Journal of Science*, *285*, 51–90. https://doi.org/10.2475/ajs.285.1.51

Lachenbruch, H. (1986). Simple models for the estimation and measurement of frictional heating by an earthquake. USGS Open File Report (pp. 86–508).

Lavallée, Y., Mitchell, T. M., Heap, M. J., Vasseur, J., Hess, K.-U., Hirose, T., & Dingwell, D. B. (2012). Experimental generation of volcanic pseudotachylytes: Constraining rheology. *Journal of Structural Geology*, *38*, 222–233. https://doi.org/10.1016/j.jsg.2012.02.001

Liang, Y. (1999). Diffusive dissolution in ternary systems: Analysis with applications to quartz and quartzite dissolution in molten silicates. *Geochimica et Cosmochimica Acta*, *63*, 3983–3995. https://doi.org/10.1016/S0016-7037(99)00203-3

Lin, A. (1994). Microlite morphology and chemistry in pseudotachylyte, from the Fuyun fault zone, China. *The Journal of Geology*, *102*, 317–329. https://doi.org/10.1086/629674

Lin, A., & Shimamoto, T. (1998). Selective melting processes as inferred from experimentally generated pseudotachylytes. *Journal of Asian Earth Science*, *16*, 533–545. https://doi.org/10.1016/S0743-9547(98)00040-3

Maddock, R. H. (1983). Melt origin of fault-generated pseudotachylytes demonstrated by textures. *Geology*, *11*, 105–108. https://doi.org/10.1130/0091-7613(1983)11<105:MOOFPD>2.0.CO;2

Malow, G., Lutze, W., & Ewing, R. C. (1984). Alteration effects and leach rates of basaltic glasses: Implications for the long-term stability of nuclear waste form borosilicate glasses. *Journal of Non-Crystalline Solids*, *67*, 305–321. https://doi.org/10.1016/0022-3093(84)90156-X

Mitchell, T., Toy, V., Di Toro, G., Renner, J., & Sibson, R. (2016). Fault welding by pseudotachylyte formation. *Geology*, *44*(12), 1059–1062. https://doi.org/10.1130/G38373.1

Moecher, D. P., & Brearley, A. J. (2004). Mineralogy and petrology of a mullite-bearing pseudotachylyte: Constraints on the temperature of coseismic frictional fusion. *American Mineralogy*, *89*, 1485–1496.

Murakami, M. (2010). Average shear work estimation of Nojima Fault from fission-track analytical data. *Earth Monthly*, *32*, 24–29.

Mysen, B. O. (1983). The structure of silicate melts. *Annual Review of Earth and Planetary Sciences*, *11*, 75–97. https://doi.org/10.1146/annurev.ea.11.050183.000451

Nestola, F., Mittempergher, S., Di Toro, G., Zorzi, F., & Pedron, D. (2010). Evidence of dmisteinbergite (hexagonal form of CaAl2Si2O8) in pseudotachylyte: A tool to constrain the thermal history of a seismic event. *American Mineralogist*, *95*, 405–409. https://doi.org/10.2138/am.2010.3393

Nielsen, S., Di Toro, G., & Griffith, W. A. (2010). Friction and roughness of a melting rock surface. *Geophysical Journal International*, *182*, 299–310. https://doi.org/10.1111/j.1365-246X.2010.04607.x

Norris, R. J., & Craw, D. (2013). *Aspiring terrane: An oceanic assemblage from New Zealand and its implications for terrane accretion in the southwest Pacific, terrane accretion and orogenic belts* (pp. 169–177). Washington, DC: American Geophysical Union.

Ohtomo, Y., & Shimamoto, T. (1994). Significance of thermal fracturing in the generation of fault gouge during rapid fault motion: An experimental verification. *Structural Geology Journal of Tectonic Research Group of Japan*, *39*, 135–144.

Rice, J. R. (2006). Heating and weakening of faults during earthquake slip. *Journal of Geophysical Research*, *111*, B50311. https://doi.org/10.1029/2005JB004006

Shaw, C. S. J. (2000). The effect of experiment geometry on the mechanism and rate of dissolution of quartz in basanite at 0.5 GPa and 1,350C. *Contributions to Mineralogy and Petrology*, *139*, 509–525. https://doi.org/10.1007/s004100000153

Shaw, C. S. J. (2004). Mechanisms and rates of quartz dissolution in melts in the CMAS (CaO-MgO-Al_2O_3-SiO_2) system. *Contributions to Mineralogy and Petrology*, *148*, 180–200. https://doi.org/10.1007/s00410-004-0581-3

Sibson, R. H. (1975). Generation of pseudotachylyte by ancient seismic faulting. *Geophysical Journal International*, *43*, 775–794. https://doi.org/10.1111/j.1365-246X.1975.tb06195.x

Smith, S. A. F., Bistacchi, A., Mitchell, T. M., Mittempergher, S., & Di Toro, G. (2013). The structure of an exhumed intraplate seismogenic fault in crystalline basement. *Tectonophysics*, *599*, 29–44. https://doi.org/10.1016/j.tecto.2013.03.031

Spagnuolo, E., Nielsen, S., Violay, M., & Di Toro, G. (2016). An empirically based steady state friction law and implications for fault stability. *Geophysical Research Letters*, *43*, 3263–3271. https://doi.org/10.1002/2016GL067881

Spray, J. G. (1987). Artificial generation of pseudotachylyte using friction welding apparatus: Simulation on a fault plane. *Journal of Structural Geology*, *9*, 49–60. https://doi.org/10.1016/0191-8141(87)90043-5

Spray, J. G. (2005). Evidence for melt lubrication during large earthquakes. *Geophysics*, *32*, 1–5.

Tagami, T. (2012). Thermochronological investigation of fault zones. *Tectonophysics*, *538*, 67–85.

Thornber, C. R., & Huebner, J. S. (1985). Dissolution of olivine in basaltic liquids; experimental observations and applications. *American Mineralogist*, *70*, 934–945.

Toy, V. G., Ritchie, S., & Sibson, R. H. (2011). Diverse habitats of pseudotachylytes in the Alpine Fault Zone and relationships to current seismicity. *Geological Society, London, Special Publications*, *359*(1), 115–133. https://doi.org/10.1144/SP359.7

Toyoshima, T. (1990). Pseudotachylyte from the Main Zone of the Hidaka metamorphic belt, Hokkaido, northern Japan. *Metamorphic Geology*, *8*, 507–523. https://doi.org/10.1111/j.1525-1314.1990.tb00483.x

Tsuchiyama, A. (1986). Melting and dissolution kinetics: Application to partial melting and dissolution of xenoliths. *Journal of Geophysical Research*, *91*, 9395–9406. https://doi.org/10.1029/JB091iB09p09395

Tsutsumi, A., & Shimamoto, T. (1997). Temperature measurements along simulated faults during seismic fault motion. *International Geology*, *5*, 223–232.

Wallace, R. C. (1976). Partial fusion along the Alpine Fault Zone, New Zealand. *Geological Society of America Bulletin*, *87*, 1225–1228. https://doi.org/10.1130/0016-7606(1976)87<1225:PFATAF>2.0.CO;2

Warr, L., & van de Pluijm, B. (2005). Crystal fractionation in the friction melts of seismic faults (Alpine Fault, New Zealand). *Tectonophysics*, *402*, 111–124. https://doi.org/10.1016/j.tecto.2004.12.034

Watson, E. B. (1994). Diffusion in volatile-bearing magmas. In M. R. Carroll & J. R. Holloway (Eds.), *Volatiles in magmas, mineralogical society of America reviews in mineralogy* (Vol. 30, pp. 371–411). Washington, DC.

Yuguchi, T., Yamaguchi, T., Iwamoto, M.-r., Eguchi, H., Isobe, H., & Nishiyama, T. (2012). Diffusion-controlled melting in granitic systems at 800-900 °C and 100-200 MPa: Temperature and pressure dependence of the minimum diffusivity in granitic melts. *Journal of Mineralogical and Petrological Sciences*, *107*, 57–73. https://doi.org/10.2465/jmps.110517

Zhang, Y., Ni, H., & Chen, Y. (2010). Diffusion data in silicate melts. *Reviews in Mineralogy and Geochemistry*, *72*, 311–408. https://doi.org/10.2138/rmg.2010.72.8

Zhang, Y., Walker, D., & Lesher, C. E. (1989). Diffusive crystal dissolution. *Contributions to Mineralogy and Petrology*, *102*, 492–513. https://doi.org/10.1007/BF00371090